The Influence of Electrode Indentation Rate on LME Formation during RSW

This paper investigates the liquid metal embrittlement cracking tendency in third-generation advanced high-strength steels during resistance spot welding

BY C. BÖHNE, G. MESCHUT, M. BIEGLER, AND M. RETHMEIER

Abstract

During resistance spot welding of zinc-coated advanced high-strength steels (AHSSs) for automotive production, liquid metal embrittlement (LME) cracking may occur in the event of a combination of various unfavorable influences. In this study, the interactions of different welding current levels and weld times on the tendency for LME cracking in third-generation AHSSs were investigated. LME manifested itself as high-penetration cracks around the circumference of the spot welds for welding currents closely below the expulsion limit. At the same time, the observed tendency for LME cracking showed no direct correlation with the overall heat input of the investigated welding processes. To identify a reliable indicator of the tendency for LME cracking, the local strain rate at the origin of the observed cracks was analyzed over the course of the welding process via finite element simulation. While the local strain rate showed a good correlation with the process-specific LME cracking tendency, it was difficult to interpret due to its discontinuous course. Therefore, based on the experimental measurement of electrode displacement during welding, electrode indentation velocity was proposed as a descriptive indicator for quantifying cracking tendency.

Keywords

- Liquid Metal Embrittlement (LME)
- Crack
- Advanced High-Strength Steel (AHSS)
- Resistance Spot Welding (RSW)
- Welding Current
- Heat Input
- Simulation

https://doi.org/10.29391/2022.101.015

Introduction

To increase driving safety and simultaneously reduce greenhouse gas emissions, the automotive industry relies on a consistent implementation of lightweight construction concepts (Ref. 1). Advanced high-strength steels (AHSSs) are highly capable of supporting this strategy due to their superior combination of elongation and tensile strength, which allow for a reduction of car body-in-white mass by downsizing the utilized sheet thickness (Ref. 2).

Resistance spot welding (RSW) is mostly used to join these steel grades (Ref. 3), which are usually coated with a zinc layer for corrosion protection. During RSW, the applied process conditions may lead to the formation of cracks caused by liquid metal embrittlement (LME) (Ref. 4). Based on the prevailing boundary conditions, the cracks can occur at different locations within a spot weld joint (Ref. 5). The assumed cause of the formation of LME is stress-assisted penetration of the liquefied zinc coating along the steel's grain boundaries, which leads to a subsequent reduction of its structural cohesion (Ref. 6). Extremely large cracks exceeding half of the sheet's thickness were shown to have a potential impact on joint properties (Refs. 7–10). Therefore, it is desirable to better understand the causes and influencing factors that lead to the formation of intense cracks.

In this context, finite element (FE) simulation of the spot welding process is an effective way to simulate temperature, stress, and strain during RSW. In previous studies, FE simulation was used to analyze and compare welding processes based on the calculated development of stresses over time

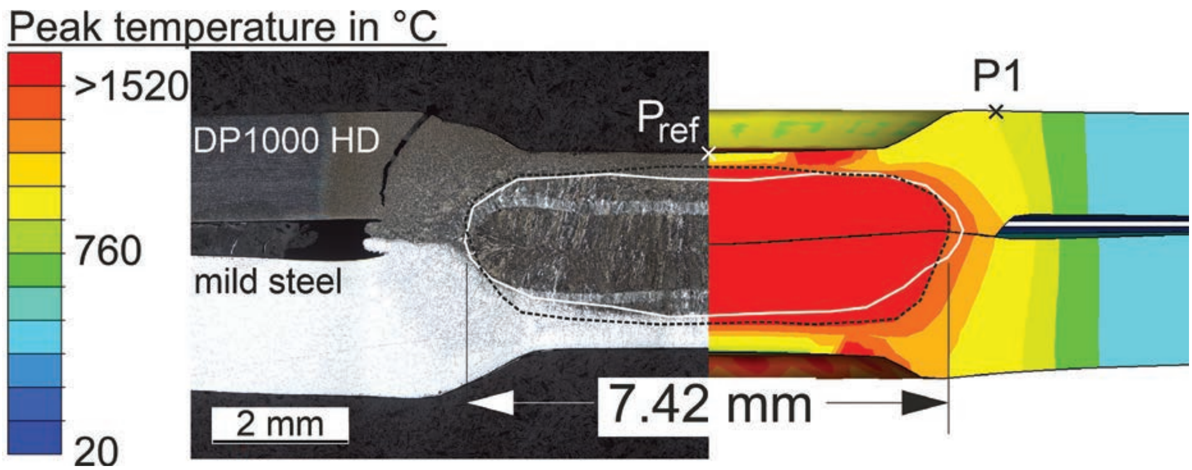

Fig. 1 — Comparison of experimental and simulated nugget shape for simulation validation. The nugget shape, height, and diameter agreed well in comparison to the experiment, and the model was considered as valid. P1 and P_{ref} were used to derive the temperature, strain rate, and electrode indentation velocity during the process.

(Refs. 11, 12) or the calculated amount of strain generated (Ref. 13).

The temperature range within which LME occurs was described by Nicholas and Old (Ref. 14) as the ductility trough. Bhattacharya et al. (Ref. 17) determined the lower end of the ductility trough to be 700°C for a dual-phase (DP) 1000 high-ductility (HD) steel via hot tensile tests. The lower end of the ductility trough may be linked to high-zinc availability, which is predicted by the Zn-Fe binary phase diagram from the melting point of intermetallic Zn-Fe phases at about 782°C (Ref. 16).

The upper end of the ductility trough is found in various hot tensile tests (Ref. 6) across materials at the evaporation temperature of Zn. This is due to the comparatively slow speed of the hot tensile test, which allows the Zn to evaporate during the test. In contrast, previous investigations (Ref. 18) of real RSW processes indicated that this limit can be exceeded for a short time without affecting the LME slope; therefore, its significance can be neglected. Likewise, hot tensile tests show that the strain rate also exerts a significant influence on the formation of LME (Ref. 19).

In deviation from the lower limit of the ductility trough determined by hot tensile tests, Wintjes et al. (Ref. 15) based their definition of the LME active region on the elemental zinc melting temperature.

Regarding the actual RSW process, the type of material combination seems to fundamentally influence crack formation. Several studies mention the increased LME susceptibility of dissimilar combinations consisting of higher sheet thickness or multiple layers (Refs. 15, 20, 21). This is caused by two effects: 1) With an increase in the total sheet thickness, it becomes necessary to introduce a greater amount of energy into the joint; and 2) in dissimilar combinations, the nugget formation is shifted into the AHSS joining partner due to its higher resistivity. Both effects support an increased heat generation within the AHSS, which has been found by several studies to be associated with increased crack formation (Refs. 22, 23). The main factor determining the heat input is the welding current, which promotes a crack formation at values close to or above the spatter limit (Refs. 24, 25). Secondly, the combination of high welding currents with excessive weld times may maximize the heat input and thus favor the formation of LME cracks (Ref. 26). Several works focus on process optimization for LME mitigation and suggest using larger working-plane electrode caps (Refs. 27, 28).

This work took as its starting point the previous reports on a connection between crack formation and increased heat input due to high welding currents and extended weld times. By fine-tuning the experimental boundary conditions, this research unveiled new analyses and may help identify previously hidden cause-effect relationships regarding strain rates and electrode indentation velocities. The electrode indentation velocity was identified as an easily measurable value that correlates with the crack occurrence. The goal was to supplement previous findings on factors influencing LME crack formation and contribute to the quantification of LME influencing factors.

Table 1 — Overview of the Experimental Setup

Stack Up	Top Sheet	DP1000 HD, t = 1.58 mm		
	Bottom Sheet	Mild steel, t = 2.00 mm		
Electrode Geometry		ISO 5281: F1-16-20-50-5.5		
Electrode Force		4.5 kN		
Squeeze/Hold Time		300 ms		
Weld Times		760 ms, 1520 ms		
Weld Current Stages		I_{min} ($d_w = 4\sqrt{t}$)	$I_{standard}$ ($d_w = 5\sqrt{t}$)	I_{max} – 0.2 kA
Weld Current per Stage at Weld Time of 760 ms		7.2 kA	8.0 kA	9.2 kA
Weld Current per Stage at Weld Time of 1520 ms		7.0 kA		

Materials and Methods

Materials

An electrogalvanized DP steel of the strength class 1000 MPa (hereinafter called DP1000 HD; corresponds to VDA 239-100 material specification: CR850Y980T-DH) was used as the investigated third-generation AHSS material for the experiments. It has a yield strength of 760 MPa, an ultimate tensile strength of 1030 MPa, and a sheet thickness of 1.58 mm. The DP1000 HD was joined with a hot-dip galvanized 2.00-mm-thick mild steel (hereinafter called mild steel) with a yield strength of 170 MPa and an ultimate tensile strength of 310 MPa. Based on these materials, a two-sheet stack up was formed consisting of the DP1000 HD as the top sheet and the mild steel as the base sheet (Table 1).

Welding Equipment and Experimental Design

RSW was performed on a servo-electric pedestal x-type welding gun using 1000-Hz medium frequency direct current (MFDC). An external weld process recorder in combination with various sensors was used to record the history of the current, voltage, force, and displacement during the welding processes. The displacement was captured via an optical laser distance sensor (LDS) and represented the movement of the upper electrode in relation to the surface of the top sheet, similarly to the research conducted in Xia et al. (Ref. 29). The measuring location was 19.0 mm outside of the center of the electrodes. The electrodes were water cooled by a rate of 4 L/min. Type F1-16-20-50-5.5 electrode caps (hereinafter called F1-5.5), as specified in ISO 5821, *Resistance welding — Spot welding electrode caps*, were used (Ref. 30).

The experimental design is shown in Table 1 and is based on welding conditions that were identified to typically cause intense LME formation, e.g., prolonged weld times of 760 and 1520 ms (Ref. 13). The resistance spot welds generated by using two different weld times, each welded with three different welding currents, were compared.

Throughout all trials, an electrode force of 4.5 kN along with a squeeze time and hold time of 300 ms were applied. The minimum (I_{min}) and maximum (I_{max}) spatter-free welding currents were determined based on common industry standards (Ref. 31). To ensure spatter-free welds, the welding current I_{max} was set to 200 A below the maximum spatter-free welding current. The nominal current ($I_{standard}$) was defined to produce a weld nugget diameter of $5\sqrt{(t)}$, which equaled 6.3 mm. The investigations were performed on a specimen of 45 × 45 mm², and ten repetitions were used per factor. To confirm LME as the cause of crack formation, reference welds were carried out on dezinced sheets under identical boundary conditions. All reference welds were completely free of cracks so that LME could be assumed to be the underlying cracking mechanism.

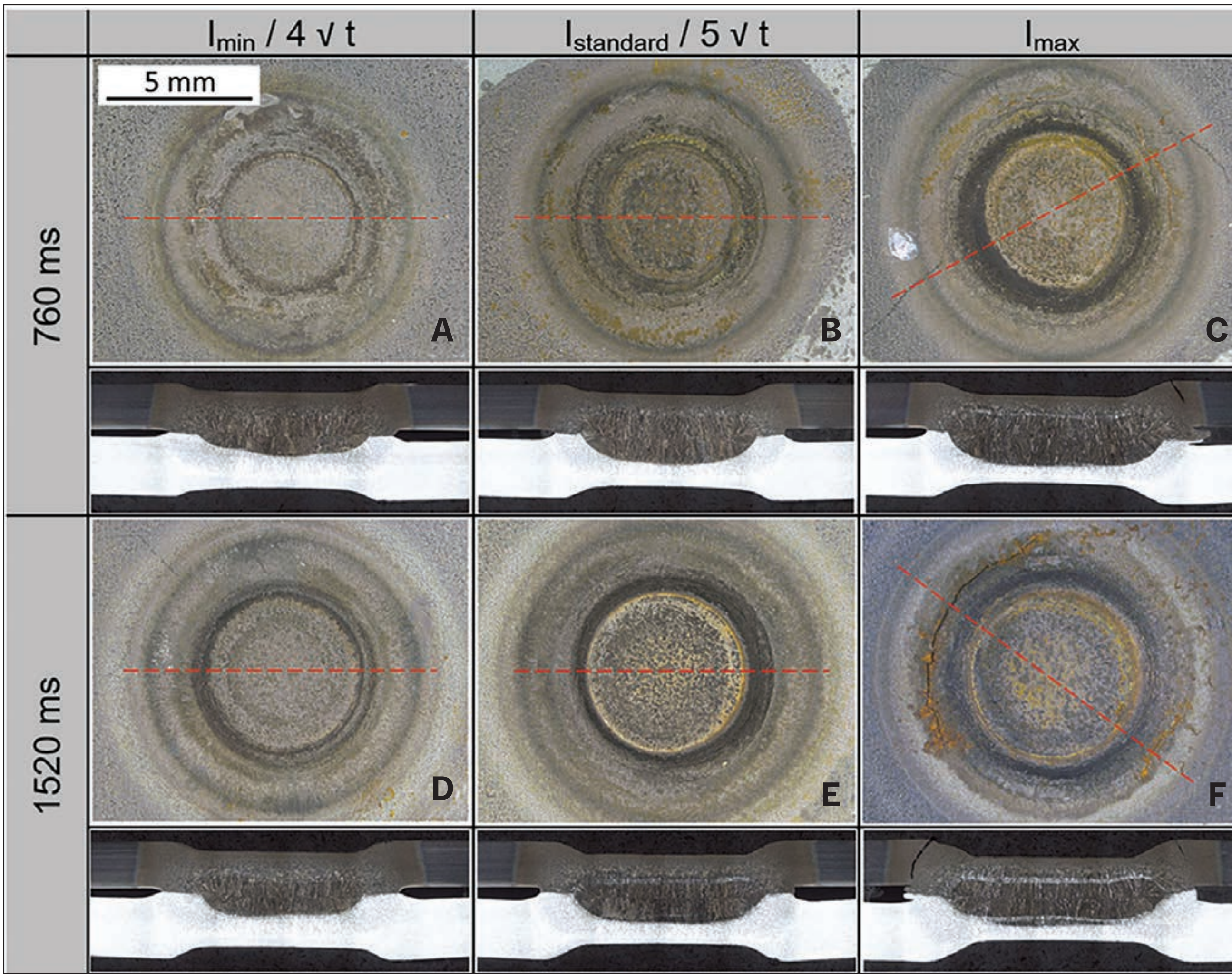

Fig. 2 — Representative top views and metallographic cross sections for welding processes A–F: Shoulder cracking (type C) is visible for processes C and F, but no cracks are visible for welding processes A, B, D, and E.

Analysis and Measuring Methods

For the verification of cracks, the zinc coating was removed around each spot weld after welding by staining with 20% hydrochloric acid and visual inspections. Photographic documentations were also carried out. The specimens were cross sectioned through the middle region of the observed cracks based on the surface crack appearance. If no cracks were observed in the surface view, the direction was chosen to be identical to the samples that showed cracks. An analysis of the accumulated visible surface crack length via an image editing software (ImageJ) was used to quantify the intensity of cracking within the specimens.

For the numerical simulations of the RSW process, the commercial FE simulation software Simufact Welding 2020 was used. A 3D electrothermomechanical model was validated against experimental temperature measurements and metallographic cross sections in Frei et al. (Ref. 32). To adjust the model for the welds in this research, the material properties determined by Schwenk and Rethmeier (Ref. 33) were scaled to the flow and yield stresses of 760 and 1030 MPa, respectively. In addition, the contact resistance was determined for the stack up at room temperature according to the DVS 2929, *Instruction sheet for measurement of contact resistance — Fundamentals, measurement methods and equipment* (Ref. 34), guideline and resulted in 37 $\mu\Omega$ for the electrode/DP1000 HD contact, 136 $\mu\Omega$ between the sheets, and 10 $\mu\Omega$ for the electrode/mild steel contact. The model was solved with a spatial meshing of 0.25-mm edge length cubic hexahedral elements in the region of interest around the weld and a time-stepping increment of 0.01 s during welding and cooling. With the material and contact resistance input data, the experimental welding parameters were input into the simulation model for $I_{standard}$ and I_{max} cases with the parameters from Table 1.

The comparison of cross sections between simulation and experiment is shown in Fig. 1 for the I_{max} 1520 ms (Fig. 2F) case. The calculated and experimental nugget sizes corresponded well with a diameter of 7.42 mm. The calculated indentation depths and shapes matched the cross sections. The simulation tended to overestimate the nugget height slightly, but this was mostly confined to the mild steel welding partner that was not of interest during this investigation. Peak temperatures were observed at the weld's surface because, as

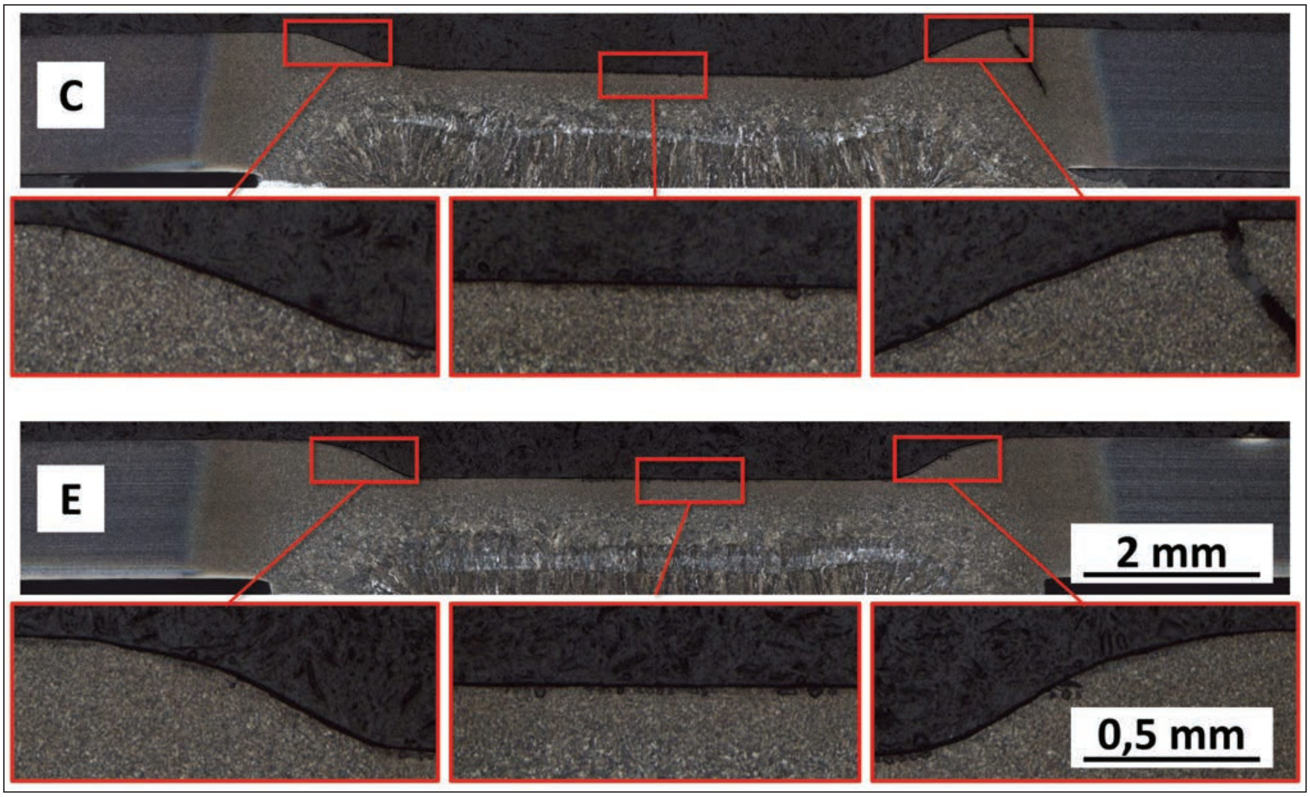

Fig. 3 — Details in metallographic cross sections for welding processes C and E. Highlighted are the absence of cracks for welding process E and the formation of cracks at the weld shoulder (type C) for welding process C during welding below expulsion.

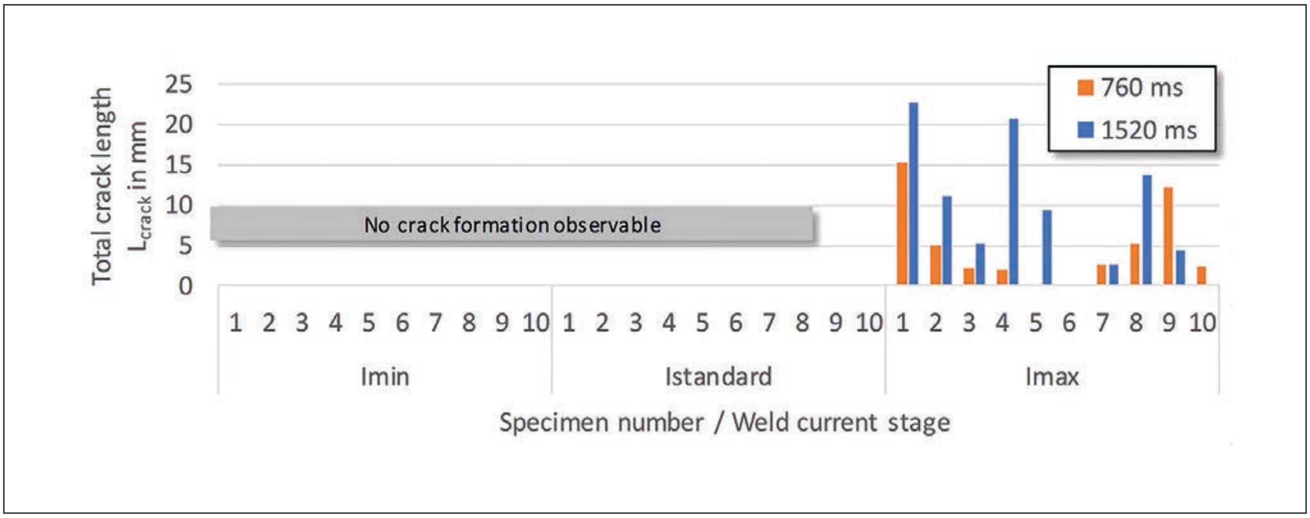

Fig. 4 — Results of the surface crack length analysis: Total crack length L_{crack}. Cracking was only observed in the I_{max} cases for weld times of 760 (welding process C) and 1520 ms (welding process F). All other trials were free of cracks for all ten repetitions.

the first current flowed, the interface was heated very briefly above melting temperature before the nugget formed. This observation corresponded to the experimental phenomenon of the electrodes sticking to the sheets after welding.

Figure 1 also shows the location of the measuring point used to extract and compare temperatures and strain rates in this work (P1). It was located 0.5 mm from the edge of the indentation in the highest-energy welding case in the region where cracking was believed to be most influential on the performance of the resistance spot weld (Ref. 7). The strain rate was calculated as the combined mechanical and thermal first derivative of the localized strain. The electrode

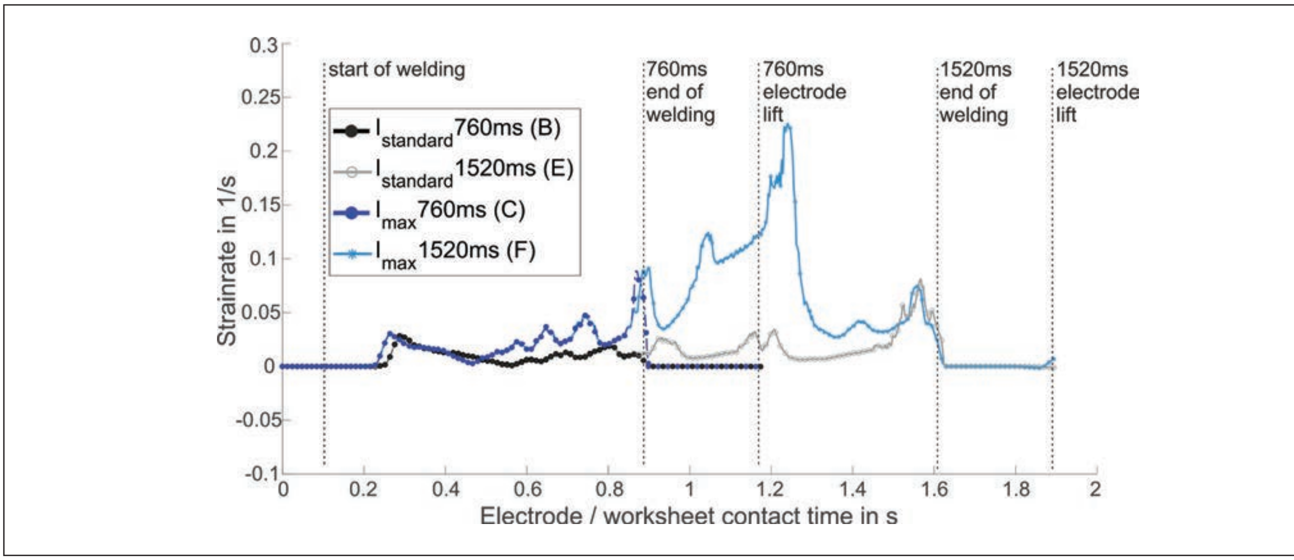

Fig. 5 — Uniaxial strain rates extracted from the numerical simulation at P1 for the welding processes B, C, E, and F. Welding processes C and F showed overall increased strain rates. All strain rates fluctuated strongly over the course of the welding processes and thus could not be easily represented by a single characteristic parameter.

Table 2 — Values for Weld Current (I), Nugget Diameter (d_n), Electrode Indentation in the Upper Sheet (e_u), Introduced Energy (Q_{IN}), and Total Crack Length (L_{crack} – $average^{max}_{min}$) for Welding Processes A–F

	Weld Current (kA)	Nugget Diameter (mm)	Electrode Indentation in the Upper Sheet (mm)	Total Heat Input (J)	Total Crack Length (mm)
I_{min} 760 ms (A)	7.2	5.89	0.27	5478	0.00 $^{0.00}_{0.00}$
$I_{standard}$ 760 ms (B)	8.0	6.18	0.40	6128	0.00 $^{0.00}_{0.00}$
I_{max} 760 ms (C)	9.2	7.45	0.51	7679	4.71 $^{15.27}_{0.00}$
I_{min} 1520 ms (D)	7.0	5.49	0.37	9348	0.00 $^{0.00}_{0.00}$
$I_{standard}$ 1520 ms (E)	8.0	6.72	0.48	11,493	0.00 $^{0.00}_{0.00}$
I_{max} 1520 ms (F)	9.2	7.42	0.59	13,962	8.97 $^{22.60}_{0.00}$

displacement was extracted from the simulation by forming the difference between the lowest point in the indentation P_{ref} and P1 for each time step. This measure accounted for the bending apart of the sheets during welding as well as the electrode sink-in. It also most closely corresponded to the optical measurements for electrode displacement undertaken in this work.

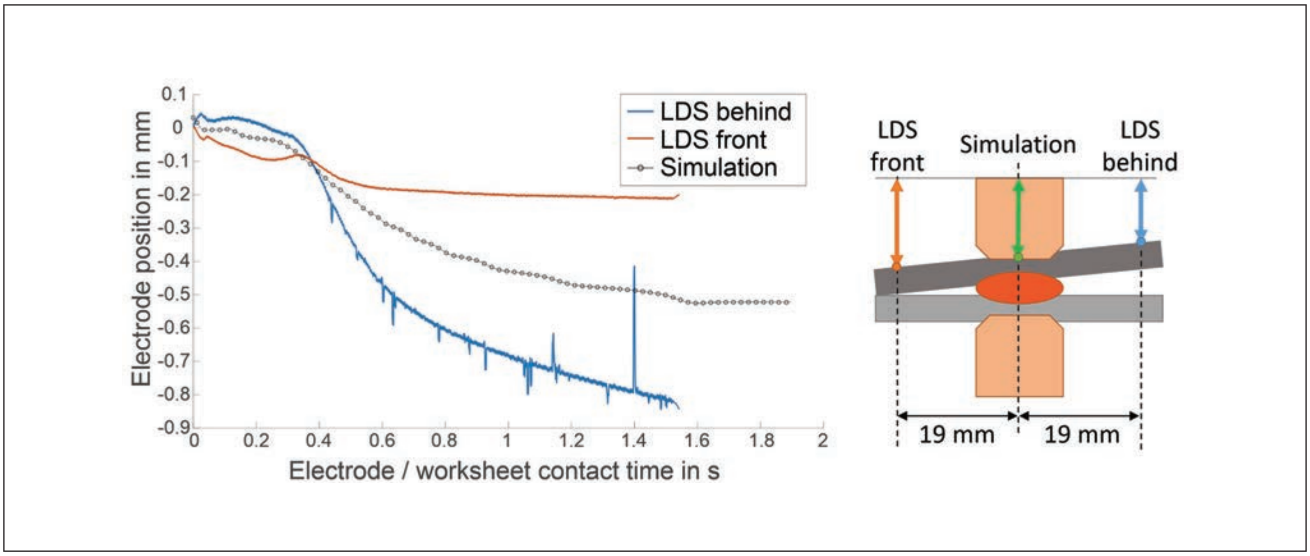

Fig. 6 — Comparison of experimentally measured (orange and blue) and simulated (gray circles) electrode sink-in behavior. Experimental curves were recorded for two distinct LDS positions: in front of the electrodes, i.e., outside of the welding gun window (LDS front, orange), and behind the electrodes, i.e., inside of the weld gun window (LDS behind, blue).

Table 3 — Duration of Exposure to Liquid Zinc t_{exp}*

Duration of Exposure to Liquid Zinc (t_{exp})→	t_{exp} (T > 420°C)	t_{exp} (T > 700°C)
$I_{standard}$ 760 ms (B)	1.84 s	0.46 s
$I_{standard}$ 1520 ms (E)	3.65 s	1.21 s
I_{max} 760 ms (C)	2.18 s	0.55 s
I_{max} 1520 ms (F)	3.79 s	1.29 s

*The time span for which the P1 was above the LME-relevant threshold temperatures of 420 and 700°C, respectively, for welding processes B, C, E, and F and LME formation could be expected. In general, t_{exp} more than doubled when changing the weld time from 760 to 1520 ms, but very little increase was observed between welding processes at standard and maximum welding currents at similar weld times.

Results and Discussion

Figure 2 shows the results of the investigations of the three current levels considered for both weld times. Each combination of weld time and welding current (Figs. 2A–F) is illustrated by a representative top view and the corresponding metallographic cross section. The nugget diameter d_n and the electrode indentation depth in the LME test material e_u (both according to Ref. 35) as well as the amount of energy Q_{IN} supplied in the respective welding process are shown in Table 2 for each case. An increase in the current intensity caused an increase in e_u for both weld times. The nugget diameter increased strongly from I_{min} to I_{max} and clearly exceeded the working plane diameter of the electrode caps used.

Figure 3 provides high-resolution cross sections to highlight the crack behavior for welding processes C and E. Figure 4 shows the evaluation of the crack length of all welding-current-time combinations. Generally, LME cracks in the center of the electrode indentation were formed during excessive heat input (beyond expulsion) for almost all types of AHSSs. The investigated steel showed exceptional behavior because only a crack formation outside of the indentation (i.e., at the weld shoulder) was noticed prior to expulsion. This observation is in accordance with the previous results reported by Böhne et al. for a similar third-generation AHSS material (Ref. 13). Cracks in the weld center can also form for these materials if the welding current is raised beyond expulsion or if the hold time is shortened excessively (Ref. 18).

Cracks could only be observed for both weld times at maximum welding current for welding processes C and F in Fig. 3. The crack length determined for the weld time 1520 ms was almost doubled compared to 760 ms.

The crack formation did not correlate with the continuously increasing energy input Q_{IN} from A to F in Fig. 2: The crack-free joint (D) created with I_{min} at 1520 ms showed a 24% increase in energy input compared to the crack afflicted joint (C) created with I_{max} at 760 ms. Nevertheless, only the latter case showed a clear crack formation, while the first parametrization reproducibly allowed the creation of crack-free joints. From here on, the I_{min} cases will no longer be considered because they were consistently free of LME.

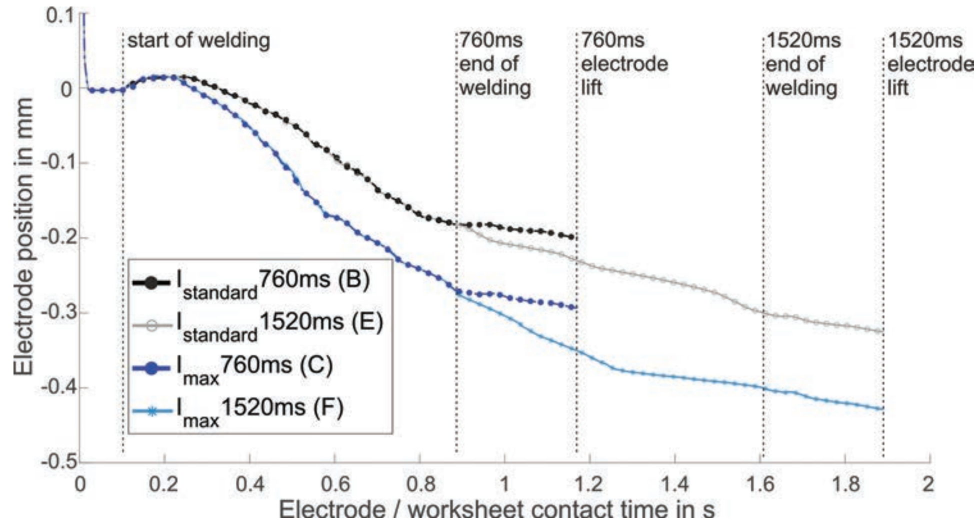

Fig. 7 — Plots of the electrode indentation formation for welding processes B, C, E, and F as calculated by FE simulation. The I_{max} welding processes (C and F) exhibited a faster sink-in behavior in comparison to the $I_{standard}$ welding processes (B and E). The final electrode positions were almost identical for the $I_{standard}$ 1520-ms welding process (E) and the I_{max} 760-ms welding process (C).

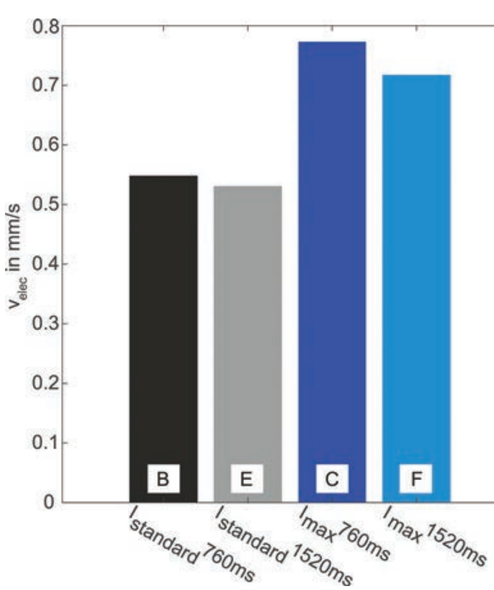

Fig. 8 — Average electrode indentation velocity v_{elec} for $I_{standard}$ (cases B and E) and I_{max} (cases C and F) according to Fig. 7. v_{elec} provides a representative and comparable metric to evaluate the characteristic electrode indentation behavior of the investigated welding processes. It can be observed that the lower welding current in B and E led to a significantly reduced electrode indentation velocity.

Table 3 contains the duration of exposure to liquid zinc t_{exp}, i.e., the time span for which the point of interest (P1) was above the LME-relevant threshold temperatures 420°C (LME-active region, Ref. 15) and > 700°C (hot tensile tests; Refs. 14, 17). The times above threshold temperatures were not significantly changed between the two welding currents at the same weld times. The most pronounced change was in the range of a 20% increase between the $I_{standard}$ and I_{max} cases for the 760 ms weld time. Moreover, the LME-afflicted case (C) experienced far shorter critical zinc times than the LME-free case (E).

Hence, the increase in heat input mentioned in van der Aa et al. (Ref. 36) could not be the only relevant influence on crack formation. Likewise, the explanatory approach used in Böhne et al. (Ref. 13) and based on the duration of exposure to liquid zinc could not justify these observations.

A comparison of the metallographic cross sections showed a slight difference in the observed electrode indentation depth in the LME test material between joints B and C. This led to the assumption that, at higher welding currents, an increased indentation or plastic deformation of the test material occurs, which leads to crack formation. Although this thesis can be used as an approach to explain the comparison considered here, it cannot justify why the joints created at 1520 ms and $I_{standard}$ (E), which show comparable indentation formation in the LME test material, did not crack in contrast to the 760 ms weld time and I_{max} (C).

A strain rate dependency of LME cracking was observed in previous work by Béal (Ref. 19). According to Kim et al. (Ref. 12), this effect may be related to the Fe-Zn reactions during hot tensile testing. For lower strain rates, an α-Fe(Zn) layer can be formed on the bulk steel, which can mitigate LME by preventing direct contact of liquid zinc and the steel's surface. Higher strain rates may fragment the α-Fe(Zn) layer and allow contact between liquid Zn and the steel, thus promoting LME cracking.

These observations led to the hypothesis that the absolute indentation depth after the process might not suffice as an influence factor for LME, but a deformation rate must be considered. Hence, the uniaxial strain rates were extracted from the numerical process simulation at P1 and compared in Fig. 5.

It is clearly visible that the I_{max} cases exhibited far greater strain rates than the $I_{standard}$ parametrization for both weld times. Even the shorter weld time of 760 ms with increased current caused significantly larger strain rates over time than the 1520 ms weld time with the standard current. Because RSW is nonlinear and governed by various equilibria of temperatures, thermal expansions, and internal/external forces, the strain rates during the processes fluctuated strongly. Furthermore, they were very difficult to measure experimentally, especially as close to the electrode indentation as was necessary for the crack-afflicted P1.

To reach a quantifiable and meaningful reference value for strain rates and evaluate their influence on LME formation, the electrode cap sink-in over the process was considered. In conjunction with thermal expansion and phase transformation volume changes, the electrode sink-in is a main driving factor for the formation of strains around the weld (Refs. 27, 29). An experimental procedure using an LDS (see section titled Analysis and Measuring Methods in this paper) was implemented by attaching the sensor to the upper electrode shaft either on the side facing the user (front) or the welding gun (behind). The setup and results are depicted in Fig. 6 for case E. Both experimental curves exhibited a short moment of upward expansion and then a sink-in of –0.2 and –0.8 mm, respectively.

The experimentally determined curves deviated from each other in a systematic way due to the test setup. The combination of high-energy welding parameters and the x-type welding gun used caused reproducible material squeezing to the rear (LDS behind) into the joint gap due to a shifting of the electrodes. This material squeezing caused a one-sided lifting (i.e., tilting) of the top sheet, which systematically reduced the measured value at the front position (LDS front) and increased it at the rear position (LDS behind). The measurement deviations compensated each other considering the symmetrical position of both measuring points around the P_{ref} measuring point of the simulation on the electrode axis. The calculated electrode position corresponded to this average of both experimental measurements in good approximation.

For further investigations, it was decided to use scatter-free simulation data for the electrode sink-in evaluations. The electrode sink-in was determined by forming the difference between the lowest point P_{ref} in the indentation and P1 in the height direction.

Figure 6 shows the results for the electrode sink-in of the $I_{standard}$ and I_{max} cases as calculated by FE simulation. For all parameters, the indentation formed during the weld time and stayed constant during holding. The 1520-ms weld time cases exhibited strong sink-in at the beginning of the weld that slowed down toward the end. A clear difference can be observed in the time taken to reach the maximum indentation depth. When I_{max} was used, the electrode indentation formed over almost the entire weld time of 760 ms with notably greater velocity. For $I_{standard}$, the most significant increase was also seen during this period, albeit slower. In the subsequent period up to 1520 ms, the indentation depth increased only marginally.

As shown in Fig. 7, the electrode indentation velocities did not progress linearly but instead decreased over the course of the welding process. High and thus critical indentation speeds were observed rather early after the start of welding. Near the end of the weld and during postweld hold time, the low movement rates were expected to be uncritical toward LME formation (Refs. 6, 19). In addition, the later the indentation formed during welding, the smaller the time window where liquid zinc was available together with the straining of the grain boundaries. To reach a quantifiable and easy-to-measure reference value for straining of the surface, the average electrode movement over the time it takes to reach a certain threshold displacement was proposed. This threshold was defined at 70% of the maximum indentation depth according to preliminary trials.

This threshold value allows for the comparison of welding processes with differing weld times by compensating for the more pronounced decrease in electrode indentation velocity over the course of longer welding processes:

$$v_{elec} = \frac{0.7 * d_{elecMax}}{t_{weld}\{0.7 * d_{elecMax}\}}$$

with v_{elec} denoting the average electrode indentation velocity in mm/s, $d_{elecMax}$ being the maximum electrode sink-in measured between the lowest point of the indentation, and P1 in mm and $t_{weld}\{0.7 * d_{elecMax}\}$ denoting the weld time necessary to reach 70% of $d_{elecMax}$. In Fig. 8, v_{elec} shows a clear increase for I_{max}, providing an explanation as to why the maximum welding cases were more susceptible to LME even though the energy input was lower in total.

The introduction of v_{elec} also provided another perspective on the reduction of LME with the increase of electrode working planes observed by DiGiovanni et al. (Ref. 28) and Murugan et al. (Ref. 27). As the larger electrode working planes led to a lowered contact stress, even while keeping the weld nugget the same size, the average electrode sink-in speed was lowered, leading to a reduced amount of LME in the weld. The higher v_{elec} value for case C in comparison to case F along with the larger observed cracks in case F (Table 2) contradicted this finding. Considering that the duration of exposure to liquid zinc t_{exp} (Table 3) more than doubled between cases C and F, the enhanced time for high-temperature zinc diffusion increased the crack occurrence.

In this context, further reference can be made to the results of Ashiri et al. (Ref. 22). They observed a reduced crack occurrence for an innovative welding schedule consisting of first a longer pulse at I_{min} and a short second pulse at I_{max}. Following the observations described in this article, the crack reducing effect of their welding schedule can be interpreted as the effect of a reduced indentation velocity by smart adaption of the welding current.

Conclusions

This study detailed publications dealing with welding process-influencing factors on LME formation during RSW. In this context, high-energy RSW scenarios of zinc-coated AHSS grades were investigated, and the occurring effects were analyzed by FE simulation. Different levels of heat input were realized by combining elongated weld times and varying welding currents. It was shown that the observed crack intensity did not necessarily increase with the amount of energy applied. Previous assumptions could be further substantiated by correlating the electrode indentation velocity as a relevant measure for crack formation, which can support the prospective development of a crack criterion.

LDS measurements were used for experimental verification. With this measuring method, systematically deviating results have been obtained depending on the measuring point due to a tilting of the top sheet. To compensate for this effect in the future, optical tracking of the electrode cap or reading the electrode drive data with adjustments for electrode cap stiffness could be implemented for consistent in-process observation.

The average electrode indentation speed value v_{elec} was proposed to quantify the straining of the material and showed good correlation with the observed LME occurrence. The value is meant to facilitate comparisons between different LME-relevant welding cases and different materials. It will need to be investigated and compared between RSW cases.

Acknowledgments

This work was funded by the Deutsche Forschungsgemeinschaft (DFG, German Research Foundation) Project ID 426686311 (Grant No. RE 1648/11-1 and ME 1840/12-1).

Disclosure Statement

No potential conflict of interest was reported by the authors.

References

1. Meschut, G., Matzke, M., Hoerhold, R., and Olfermann, T. 2014. Hybrid technologies for joining ultra-high-strength boron steels with aluminum alloys for lightweight car body structures. *Procedia CIRP* 23: 19–23. DOI: 10.1016/j.procir.2014.10.089

2. Schmitt, J.-H., and Lung, T. 2018. New developments of advanced high-strength steels for automotive applications. *Comptes Rendus Physique* 19(8): 641–656. DOI: 10.1016/j.crhy.2018.11.004

3. Manladan, S. M., Abdullahi, I., and Hamza, M. F. 2015. A review on the application of resistance spot welding of automotive sheets. *Journal of Engineering and Technology* 10(2): 20–37.

4. Ling, Z., Wang, M., and Kong, L. 2018. Liquid metal embrittlement of galvanized steels during industrial processing: A review. *Transactions on Intelligent Welding Manufacturing*: 25–42. DOI: 10.1007/978-981-10-8330-3_2

5. Murugan, S. P., Park, Y.-D., Vijayan, V., and Ji, C. 2020. Four types of LME cracks in RSW of Zn-coated AHSS. *Welding Journal* 99(3): 75-s to 92-s. DOI: 10.29391/2020.99.008

6. Bhattacharya, D. 2018. Liquid metal embrittlement during resistance spot welding of Zn-coated high-strength steels. *Materials Science and Technology* 34(15): 1809–1829. DOI: 10.1080/02670836.2018.1461595

7. Choi, D., Uhm, S., Enloe, C., Lee, H., and Kim, G. 2017. Liquid metal embrittlement of resistance spot welded 1180TRIP steel — Effects of crack geometry on weld mechanical performance. *Materials Science & Technology 2017 Conference & Exhibition (MS&T17)*: 454–462. DOI: 10.7449/2017/MST_2017_454_462

8. DiGiovanni, C., Han, X., Powell, A., Biro, E., and Zhou, N. Y. 2019. Experimental and numerical analysis of liquid metal embrittlement crack location. *Journal of Materials Engineering and Performance* 28(4): 2045–2052. DOI: 10.1007/s11665-019-04005-2

9. DiGiovanni, C., Biro, E., and Zhou, N. Y. 2019. Impact of liquid metal embrittlement cracks on resistance spot weld static strength. *Science and Technology of Welding and Joining* 24(3): 218–224. DOI: 10.1080/13621718.2018.1518363

10. Jang, G. H., Kwon, K., Kim, W., Uhm, S., Lee, T., and Lee, C. S. 2021. Effect of type-B liquid metal embrittlement cracks on high-cycle fatigue properties of spot-welded 1180 TRIP steel. *Science and Technology of Welding and Joining* 26(2): 173–179. DOI: 10.1080/13621718.2021.1872289

11. Choi, D.-Y., Sharma, A., and Jung, J. P. 2018. Parametric study for liquid metal embrittlement in resistance spot welds of galvanized trip steel. *Proceedings of the Sheet Metal Welding Conference XVIII*, 1–9. Livonia, Mich.

12. Kim, J.-U., Murugan, S. P., Kim, J.-S., Yook, W., Lee, C.-Y., Ji, C., Jeon, J. B., and Park, Y.-D. 2021. Liquid metal embrittlement during the resistance spot welding of galvannealed steels: Synergy of liquid Zn, α-Fe(Zn) and tensile stress. *Science and Technology of Welding and Joining* 26(3): 196–204. DOI: 10.1080/13621718.2021.1880816

13. Böhne, C., Meschut, G., Biegler, M., Frei, J., and Rethmeier, M. 2019. Prevention of liquid metal embrittlement cracks in resistance spot welds by adaption of electrode geometry. *Science and Technology of Welding and Joining* 39(4): 1–8. DOI: 10.1080/13621718.2019.1693731

14. Nicholas, M. G., and Old, C. F. 1979. Liquid metal embrittlement. *Journal of Materials Science* 14: 1–18. DOI: 10.1007/BF01028323

15. Wintjes, E., DiGiovanni, C., He, L., Bag, S., Goodwin, F., Biro, E., and Zhou, Y. 2019. Effect of multiple pulse resistance spot welding schedules on liquid metal embrittlement severity. *Journal of Manufacturing Science and Engineering* 141(10): 101001. DOI: 10.1115/1.4044099

16. Marder, A. R. 2000. The metallurgy of zinc-coated steel. *Progress in Materials Science* 45(3): 191–271. DOI: 10.1016/S0079-6425(98)00006-1

17. Bhattacharya, D., Findley, K., Ghassemi-Armaki, H., Speer, J., and Aa, E. M. 2018. Quantitative assessment of the characteristics of liquid metal embrittlement during resistance spot welding of Zn-coated high-strength steels. *Proceedings of the Sheet Metal Welding Conference XVIII*, 1–10. Livonia, Mich.

18. Böhne, C., Meschut, G., Biegler, M., and Rethmeier, M. 2020. Avoidance of liquid metal embrittlement during resistance spot welding by heat input dependent hold time adaption. *Science and Technology of Welding and Joining* 25(7): 617–624. DOI: 10.1080/13621718.2019.1693731

19. Béal, C. 2011. Mechanical behaviour of a new automotive high manganese TWIP steel in the presence of liquid zinc. PhD diss., INSA de Lyon, Villeurbanne, France.

20. Benlatreche, Y., Dupuy, T., and Mescolini, D. 2019. Design rules to minimize liquid metal embrittlement (LME) cracking. *Joining in Car Body Engineering*. Automotive Circle: Hannover, Germany.

21. Fritzsche, C. 2019. Prüfmethoden zur charakterisierung des auftretens von LME beim widerstandspunktschweißen von stählen [Test methods for characterizing the occurrence of LME during resistance spot welding of steels]. 24 DVS-Sondertagung Widerstandsschweißen [*24th DVS Special Conference on Resistance Welding*]: 171–183.

22. Ashiri, R., Shamanian, M., Salimijazi, H. R., Haque, M. A., Bae, J.-H., Ji, C.-W., Chin, K.-G., and Park, Y.-D. 2016. Liquid metal embrittlement-free welds of Zn-coated twinning induced plasticity steels. *Scripta Materialia* 114: 41–47. DOI: 10.1016/j.scriptamat.2015.11.027

23. DiGiovanni, C., and Biro, R. 2021. A review of current LME test methods and suggestions for developing a standardized test procedure. *Welding in the World* 65(5): 865–884. DOI: 10.1007/s40194-020-01050-7

24. Frei, J., and Rethmeier, M. 2018. Susceptibility of electrolytically galvanized dual-phase steel sheets to liquid metal embrittlement during resistance spot welding. *Welding in the World* 62(5): 1031–1037. DOI: 10.1007/s40194-018-0619-1

25. DiGiovanni, C., Bag, S., Mehling, C., Choi, K. W., Macwan, A., Biro, E., and Zhou, N. Y. 2019. Reduction in liquid metal embrittlement cracking using weld current ramping. *Welding in the World* 63(6): 1583–1591. DOI: 10.1007/s40194-019-00790-5

26. Sierlinger, R., and Gruber, M. A cracking good story about liquid metal embrittlement during spot welding of advanced high strength steels. voestalpine Stahl GmbH.

27. Murugan, S. P., Mahmud, K., Ji, C., Jo, I., and Park, Y.-D. 2019. Critical design parameters of the electrode for liquid metal embrittlement cracking in resistance spot welding. *Welding in the World* 63(6): 1613–1632. DOI: 10.1007/s40194-019-00797-y

28. DiGiovanni, C., He, L., Pistek, U., Goodwin, F., Biro, E., and Zhou, N. Y. 2020. Role of spot weld electrode geometry on liquid metal embrittlement crack development. *Journal of Manufacturing Processes* 49: 1–9. DOI: 10.1016/j.jmapro.2019.11.015

29. Xia, Y.-J., Su, Z.-W., Lou, M., Li, Y.-B., and Carlson, B. E. 2020. Online precision measurement of weld indentation in resistance spot welding using servo gun. *IEEE Transactions on Instrumentation and Measurement* 69(7): 4465–4475. DOI: 10.1109/TIM.2019.2943981

30. DIN EN ISO 5821:2009, *Resistance welding — Spot welding electrode caps* (German version). 2009. Deutsches Institut für Normung (DIN).

31. SEP 1220-2:2011-08, *Testing and documentation guideline for the joinability of thin sheet of steel — Part 2: Resistance spot welding*. 2011. Verlag Stahleisen GmbH.

32. Frei, J., Biegler, M., Rethmeier, M., Böhne, C., and Meschut, G. 2019. Investigation of liquid metal embrittlement of dual phase steel joints by electro-thermomechanical spot-welding simulation. *Science and Technology of Welding and Joining* 90(1–10). DOI: 10.14279/depositonce-10555

33. Schwenk, C., and Rethmeier, M. 2011. Material properties for welding simulation — Measurement, analysis, and exemplary data. *Welding Journal* 90(11): 220-s to 226-s.

34. Instruction sheet for measurement of contact resistance — Fundamentals, measurement methods and equipment (German version). 2014. Merkblatt DVS 2929-1:2014-08.

35. ISO 14329:2003, *Resistance welding — Destructive tests of welds — Failure types and geometric measurements for resistance spot, seam and projection welds*. 2003. Deutsches Institut für Normung (DIN).

36. van der Aa, E., Hanlon, D. N., and van der Veldt, T. 2017. Resistance spot weldability of 3rd generation advanced high strength steels for automotive applications. *5th International Conference on Steels in Cars and Trucks*. Amsterdam-Schiphol, The Netherlands.

CHRISTOPH BÖHNE (*christoph.boehne@lwf.uni-paderborn.de*) and **GERSON MESCHUT** are with the Laboratory for Material and Joining Technology, Paderborn, Germany. **MAX BIEGLER** and **MICHAEL RETHMEIER** are with the Fraunhofer Institute for Production Systems and Design Technology, Berlin, Germany. **RETHMEIER** is also with the Federal Institute for Materials Research and Testing as well as the Institute for Machine Tools and Factory Management at Technical University of Berlin, Berlin, Germany.

Welding Journal Now Publishing Direct Object Identifier (DOI) Numbers

Dear members of the welding research community,

Note that in each issue of the *Welding Journal* Research Supplement, we are including Direct Object Identifier (DOI) numbers with each of the papers published in print and online. A direct object identifier is a unique alphanumeric string assigned by a registration agency (we are using *Crossref.org*) to identify content and provide a persistent link to its location on the Internet. Our decision to begin assigning a DOI for each paper comes directly from a request by the research community.

As part of our obligation to *Crossref.org*, we are asked to provide DOI numbers, when available, in the references section of papers. So, if you have submitted a paper to the *Welding Journal* or are planning on submitting a paper, we ask that you update your references to include DOI numbers whenever possible.

Thank you.

Annette Alonso